JACS
JOURNAL OF THE AMERICAN CHEMICAL SOCIETY
ARTICLE
pubs.acs.org/JACS

Thermoelectrics from Abundant Chemical Elements: High-Performance Nanostructured PbSe−PbS

John Androulakis,[†] Iliya Todorov,[‡] Jiaqing He,[†,§] Duck-Young Chung,[‡] Vinayak Dravid,[§] and Mercouri Kanatzidis*[,†,‡]

[†]Department of Chemistry and [§]Department of Materials Science & Engineering, Northwestern University, Evanston, Illinois 60208, United States

[‡]Materials Science Division, Argonne National Laboratory, Argonne, Illinois 60439, United States

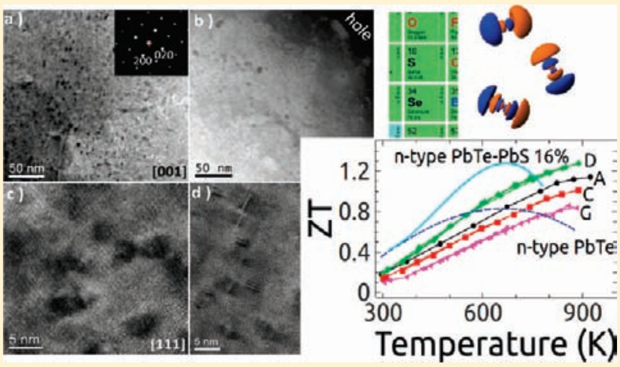

ABSTRACT: We report promising thermoelectric properties of the rock salt PbSe−PbS system which consists of chemical elements with high natural abundance. Doping with $PbCl_2$, excess Pb, and Bi gives n-type behavior without significantly perturbing the cation sublattice. Thus, despite the great extent of dissolution of PbS in PbSe, the transport properties in this system, such as carrier mobilities and power factors, are remarkably similar to those of pristine n-type PbSe in fractions as high as 16%. The unexpected finding is the presence of precipitates ∼2−5 nm in size, revealed by transmission electron microscopy, that increase in density with increasing PbS concentration, in contrast to previous reports of the occurrence of a complete solid solution in this system. We report a marked impact of the observed nanostructuring on the lattice thermal conductivity, as highlighted by contrasting the experimental values (∼1.3 W/mK) to those predicted by Klemens−Drabble theory at room temperature (∼1.6 W/mK). Our thermal conductivity results show that, unlike in PbTe, optical phonon excitations in PbSe−PbS systems contribute to heat transport at all temperatures. We show that figures of merit reaching as high as ∼1.2−1.3 at 900 K can be obtained, suggesting that large-scale applications with good conversion efficiencies are possible from systems based on abundant, inexpensive chemical elements.

INTRODUCTION

Strong interest in efficient waste heat management and energy conservation and conversion is currently driving a broad search for advanced thermoelectric materials.[1−4] Although progress in raising the efficiency has been impressive, a significant factor in the viability of modern thermoelectrics that should not be overlooked has to do with the cost and broad availability of end products, which are intimately related to materials selection. Currently, a large body of work in the so-called intermediate temperature regime (600−900 K), where a large number of broad-based applications can benefit (e.g., automotive), deals with Te-based materials such as PbTe.[1,5] However, Te is not only rare in the Earth's crust[6] but also increasingly used in a number of other applications, such as steel metallurgy, solar cells, phase change materials for digital recording, and thermoelectric cooling devices based on Bi_2Te_3.[7] Attractive Te-free alternatives to rock salt PbTe are the congeneric PbSe and PbS, which importantly have remarkably similar electronic and structural properties.[8,9] Furthermore, selenium is 50 times more abundant than tellurium,[6] while sulfur is among the 16 elements with the highest abundance in the Earth's crust.[6] To date, neither PbSe nor PbS has received the level of attention afforded to their tellurium analogue.[10−14]

Increasing focus is now beginning to be placed on PbSe and PbS systems[9,15,16] as well as other systems such as Mg_2Si and skutterudites.[17−19] Recently, we reported that slight modifications in the electronic band structure of n-type PbSe can lead to a thermoelectric figure of merit, ZT, of ∼0.9 at 900 K.[20] This figure of merit ($ZT = S^2\sigma T/\kappa$, where S the thermopower, σ the electrical conductivity, and κ the thermal conductivity) is inversely related to κ; therefore, reducing κ provides another path to increase ZT. A successful material system that demonstrates the approach of reducing κ is PbTe-PbS.[21−23] In PbTe−PbS, thermodynamically stable endotaxial nanocrystals of PbS and point defect scattering on the Te sublattice keep the phononic transport in the temperature range 300−750 K at a very low level, resulting in a ZT of ∼1.2−1.4 at 700−750 K.[21,22]

In this work we have prepared and studied $(PbSe)_{1-x}(PbS)_x$ ($0.08 \leq x \leq 0.02$) compositions, with the goal of understanding the high-temperature thermoelectric properties of this system. We have investigated whether a reduction of thermal conductivity through point defect scattering could coexist with a high power factor, $S^2\sigma$, by controlled doping with electron donors such as excess Pb, $PbCl_2$, and Bi. The choice of dopants was based on the consideration that excess of Pb creates Se vacancies and generates electrons,[20] $PbCl_2$ dopes on the anion sublattice

Received: April 2, 2011
Published: June 08, 2011

dx.doi.org/10.1021/ja203022c | J. Am. Chem. Soc. 2011, 133, 10920–10927

with Cl$^-$, and Bi dopes effectively at very low concentrations on the Pb sites.[24] Power factors up to 14 μW/cm·K^2 at 900 K were measured, similar to those extracted in pristine PbSe. Contrary to previous literature claims[25−27] of the formation of a solid solution of $(PbSe)_{1-x}(PbS)_x$ composition, our transmission electron microscopy (TEM) studies actually reveal nanostructuring through the formation of nanocrystalline PbS precipitates. The discovery of nanostructuring in the $(PbSe)_{1-x}(PbS)_x$ system is surprising since the system exhibits a linear variation of the lattice parameter with *x*, i.e., obeying Vergard's law. We show here that the microstructure of $(PbSe)_{1-x}(PbS)_x$ reduces the lattice thermal conductivity by an additional ~15% at room temperature compared to the prediction by Klemens−Drabble (KD) theory for solid solutions and umklapp-only processes. Through a detailed analysis of the high-temperature lattice thermal conductivity data, we also show that, unlike in PbTe, there is an inherent effect of excitation of heat carrying optical phonons. We report that, with optimized doping, a ZT of up to 1.3 at 900 K can be realized, signifying that good conversion efficiencies are achievable with systems based on abundant chemical elements.

EXPERIMENTAL SECTION

$(PbSe)_{1-x}(PbS)_x$ specimens were prepared by reacting high-purity Pb (American Elements, 99.999%), Se (5N Plus Inc., 99.999%), and S (5N Plus Inc., 99.985%) in evacuated silica tubes. In the case of Pb and Bi dopants, the tubes were fired at 1150 °C over a period of 12 h, soaked at that temperature for 4 h, and subsequently rapidly cooled to room temperature over a period of 4 h. Specimens doped with $PbCl_2$ were grown in a vertical single-zone Bridgman furnace after a prereaction step at 600 °C for 48 h. The study of the lattice thermal conductivity at room temperature and comparison to the predictions of KD theory[23] were performed on undoped $(PbSe)_{1-x}(PbS)_x$ ingots that were produced by rapid solidification from the melt. Two cylindrical samples with heights ~3 and 10 mm were cut one after the other along each of the produced ingots. The 3 mm thick cylinder was polished to a thickness of ~2 mm and used for thermal conductivity measurements; the 10 mm long cylinder was polished to a bar shape with typical dimensions 3 × 3 × 8 mm and used in charge transport measurements. A typical pair of specimens used in this study is shown in Figure 1a.

X-ray powder diffraction data were recorded with an INEL diffractometer equipped for Cu Kα irradiation. Powdered samples were also used to record electronic absorption spectra in the infrared region of the electromagnetic spectrum at room temperature in a Nicolet 6700 FTIR spectrometer. The spectra were used to extract the energy band gap of the samples as described previously.[15]

Microstructure investigations were carried out in a JEOL 2100F Scanning TEM or TEM (S/TEM) operating at a 200 kV accelerating voltage. The TEM samples were prepared by polishing, dimpling, and ion milling with liquid nitrogen to obtain thin sections for S/TEM analysis. Alternative specimen preparation methods, such as crushing to obtain cleaved geometry, mechanical tripod polishing, and focused ion beam (FIB), were also employed to ensure that ion beam thinning did not cause any notable changes to the overall microstructure.

The thermal diffusivity was measured with a NETZSCH LFA-457 instrument in the temperature range 300−900 K. The 2 mm cylinder disks coated with graphite were utilized in this study. The specific heat was approximated by a linear relationship taking into account the PbS concentration inside PbSe according to published values.[29] The mass densities of the samples were determined inside an AccuPyc 1340 pycnometer from Micromeritics.

A ZEM-3 instrument from Ulvac was used to simultaneously determine the electrical conductivity and Seebeck coefficient of the bar-shaped specimens at the same temperature. Samples measured to 900 K were coated with boron nitride to protect the instrument against evaporation of S, Se, and/or Pb. Multiple thermal cycles and different specimens produced similar properties. The charge transport specimens were subsequently used in room-temperature Hall effect measurements to determine their carrier densities on the assumption of a unitary Hall factor which gives a Hall coefficient $R = 1/ne$, where n is the carrier density and e the electronic charge. The apparatus is described in detail in ref 15. The $(PbSe)_{1-x}(PbS)_x$ specimens studied here were found to have carrier densities in the range (1−3.5) × 10^{19} cm^{-3} using excess Pb as dopant, (1−4.5) × 10^{19} cm^{-3} using $PbCl_2$ as dopant, and (1−7) × 10^{19}cm^{-3} for specimens doped with Bi.

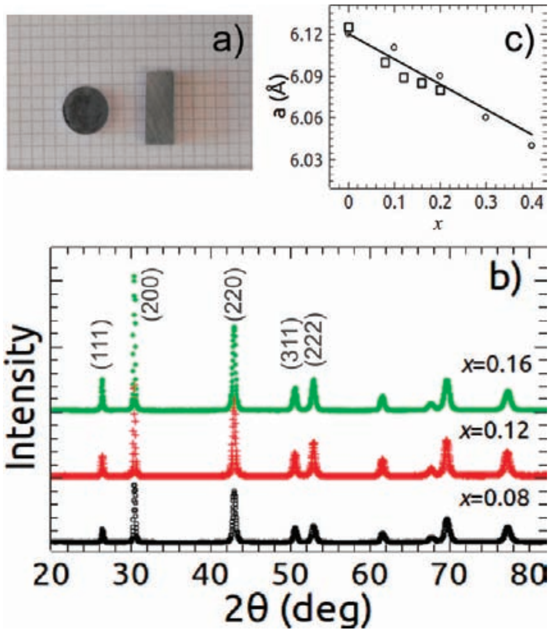

Figure 1. (a) Typical specimens used in this study. (b) Powder X-ray diffraction patterns of $(PbSe)_{1-x}(PbS)_x$ (x = 0.08, 0.12, 0.16), exhibiting a single-phase rock salt structure. (c) Extracted lattice parameters of PbSe, $(PbSe)_{1-x}(PbS)_x$ (x = 0.08, 0.12, and 0.16, □) compared with literature data (○), indicating a linear contraction of the lattice.

RESULTS AND DISCUSSION

1. Structure and Optical Properties. Figure 1b shows typical powder X-ray diffraction patterns for samples of $(PbSe)_{1-x}(PbS)_x$ (x = 0.08, 0.12, 0.16). The patterns show no detectable evidence for a second phase. The diffraction profiles were fitted with a least-squares refinement method within the $Fm\overline{3}m$ space group, and the extracted lattice parameter suggests a linearly contracting lattice from PbSe (6.125 Å) to PbS (5.930 Å) with increasing the PbS molar ratio, consistent with Vergard's law. Figure 1c is a plot of the lattice parameters determined for our samples (open squares) compared with literature data (circles).[30] The solid line represents a calculation based on solid solution behavior.

Figure 2 depicts electronic absorption spectra as functions of photon energy for x = 0, 0.08, 0.12, and 0.16. The energy band gap is clearly observable and shifts toward higher energies with increasing PbS concentration. The band gap, E_g, as a function of x at room temperature (inset of Figure 2) increases linearly from ~0.27 to 0.31 eV with increasing x. A linear fit of the data projects to an expected band gap of ~0.45 eV for PbS, which is in

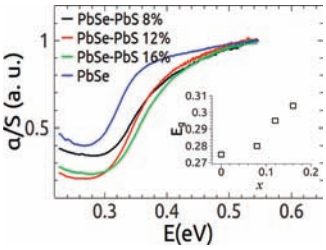

Figure 2. Electronic absorption spectra obtained from diffuse reflectance infrared spectroscopy measurements on pulverized specimens of $(PbSe)_{1-x}(PbS)_x$. The inset depicts the estimated band gap values as a function of x.

agreement with the literature value of ~0.41−0.44 eV for PbS.[8] These data are consistent with a solid solution behavior; however, as we will show for the first time, these materials actually possess significant nanoscale inhomogeneities that are critical to the transport properties.

2. Charge Transport Properties. Figure 3a depicts the electrical conductivity as a function of temperature for representative samples of the system $(PbSe)_{1-x}(PbS)_x$ doped with $PbCl_2$, Pb, and Bi. The symbols A−G on the graph correspond to Table 1, where the samples used in the present study are listed according to composition, dopant type, dopant concentration, and carrier density as measured by the Hall effect. From Table 1 we conclude that Bi has a very efficient dopant action compared to $PbCl_2$ and Bi. However, the method of production (cast ingot) of the Bi-doped sample may contribute to microstructural defects that limit the mobility, and hence its conductivity (see Figure 3a) is lower than that of sample D.

In all samples the electrical conductivity decreases with increasing temperature, consistent with heavily doped semiconductors. Modeling the electrical conductivity with a single power law dependence of the form $\sigma \sim T^{-\delta}$ is not possible. As in the case of pristine PbSe,[20] two different regions with two distinct exponents appear in $\log \sigma$−$\log T$ plots (see Figure 3b). The exponents vary with doping and temperature, most probably because of degeneracy. The high-temperature exponent δ is close to ~2.6, while the low-temperature exponent is ~1.7. The exponent values compare well with those observed in PbSe itself,[20] and since they are related to carrier mobilities at the bottom of the conduction band this is consistent with (a) the expectation that the Pb sublattice in the $(PbSe)_{1-x}(PbS)_x$ samples is unperturbed and (b) theoretical calculations that show the conduction band minimum in Pb chalcogenides is made predominantly of Pb-based s and p orbitals.[9,31,32]

Figure 4a shows the thermoelectric power, S, as a function of temperature for samples of $(PbSe)_{1-x}(PbS)_x$ doped with Pb, $PbCl_2$, and Bi. The thermoelectric power increases linearly with temperature and reaches ~ −250 μV/K at 900 K. There is no sign of saturation of thermoelectric power up to 900 K, suggesting absence of significant bipolar diffusion most probably resulting from an increased band gap as discussed above. Bipolar diffusion derives from thermal carrier excitations across the band gap at high temperatures. For pure PbSe E_g increases at a rate of 4×10^{-4} eV/K, and therefore at 900 K E_g can reach as high as 0.51 eV.[33] The addition of PbS is expected to further increase the band gap and therefore places the system well above the limiting condition for optimal performance of $E_g > 6k_BT$ at 900 K.[34] The increase in energy gap with rising temperature is anomalous and characteristic of all lead chalcogenides. The reason for this may be related to the recent discovery that the Pb atoms are in fact shifted off the octahedron center in the rock salt structure,[35] with the off-center displacement increasing with rising temperature.[35]

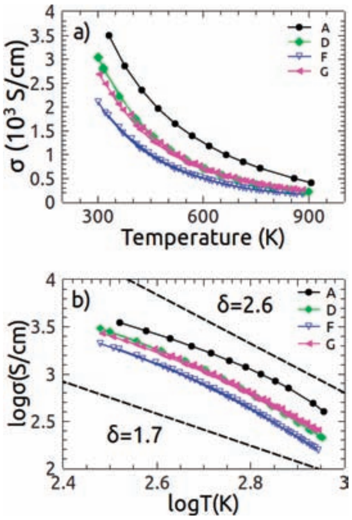

Figure 3. (a) Electrical conductivity as a function of temperature for samples A, D, F, and G. Data for samples B, C, and E have a similar behavior and are omitted for clarity. (b) $\log \sigma$−$\log T$ plots indicating two linear regimes with two different slopes. The dashed lines marked as δ = 2.6 and δ = 1.7 are guides to the eye for the high- and low-temperature intervals. A full description of samples A−G is given in Table 1.

Table 1. Samples of the Present Study Categorized on the Basis of PbS Content, Dopant Type, Dopant Concentration, and Measured Carrier Density

sample	composition	dopant, mol %	n ($\times 10^{19}$ cm^{-3})
A	$(PbSe)_{1-x}(PbS)_x$ (x = 0.08)	Pb, 0.30%	2.6
B	$(PbSe)_{1-x}(PbS)_x$ (x = 0.08)	Pb, 0.35%	2.9
C	$(PbSe)_{1-x}(PbS)_x$ (x = 0.08)	$PbCl_2$, 0.30%	2.8
D	$(PbSe)_{1-x}(PbS)_x$ (x = 0.12)	$PbCl_2$, 0.30%	2.4
E	$(PbSe)_{1-x}(PbS)_x$ (x = 0.12)	$PbCl_2$, 0.40%	4.5
F	$(PbSe)_{1-x}(PbS)_x$ (x = 0.16)	$PbCl_2$, 0.30%	2.2
G	$(PbSe)_{1-x}(PbS)_x$ (x = 0.12)	Bi, 0.30%	3.2

Since changes in the electronic structure are also reflected in the carrier's effective mass, the thermoelectric power, which is related to the effective mass, allows us to check the working hypothesis of an uninterrupted Pb sublattice that permits electrons to flow relatively undisturbed as in the pristine PbSe. To this end we have calculated the thermoelectric power as a function of carrier density at room temperature of the pristine compound PbSe. In the calculation we assumed parabolic bands and a single dominant scattering mechanism, that of electron−acoustical phonon interaction. In this approximation, the carrier density was approximated by the relationship[15,36]

$$n = 4\pi \left(\frac{2m^* k_B T}{h^2}\right)^{3/2} F_{1/2}(\eta) \tag{1}$$

and the thermoelectric power, S,

$$S = \frac{k_B}{e}\left(\frac{2F_1(\eta)}{F_0(\eta)} - \eta\right) \tag{2}$$

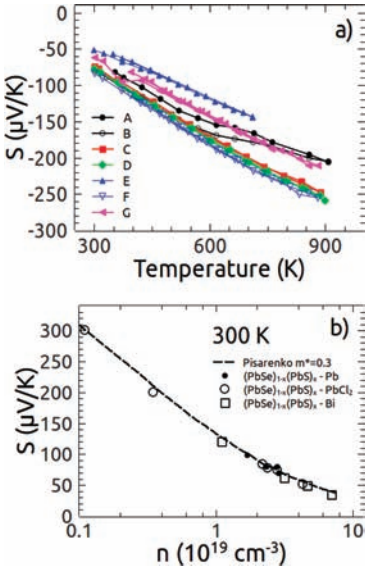

Figure 4. (a) Seebeck coefficient as a function of temperature for samples A−G. Note that a linear nonsaturating dependence on temperature is observed up to 900 K for all samples. (b) Pisarenko plot at 300 K, Seebeck vs carrier density, for samples in this study, regardless of their PbS content or dopant. The dashed black line corresponds to the theoretically expected curve for the pristine PbSe with $m^* \approx 0.3$. The excellent agreement suggests that PbS contents up to 16% and the level of dopants used do not have a marked effect in perturbing the electronic density of states of the PbSe matrix.

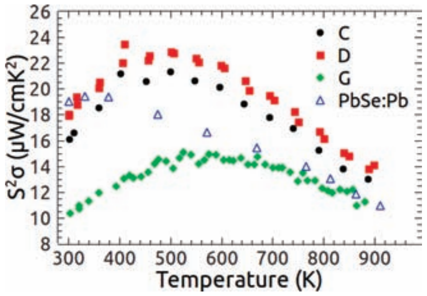

Figure 5. Power factor curves as a function of temperature for samples C, D, and G. The power factor of pristine n-type PbSe doped with excess Pb at a level of 2×10^{19} cm^{-3} is also plotted (blue triangles) for comparison.

In the above equations m^* is the effective mass, k_B the Boltzmann constant, η the reduced chemical potential, and F_i the appropriate order Fermi integral.[15,36] We note that eq 1 should be divided by the so-called Hall factor, which takes into account anisotropy of the bands and relaxation times of carriers moving along and across the principal conduction axis of the Fermi surface.[8] For parabolic bands and a spherical Fermi surface the Hall factor is unity.[8] Using eqs 1 and 2, we varied the values of η to generate n and S pairs on the assumption of an effective mass ~0.3m_o for PbSe.[37] The results are shown as the dotted line in Figure 4b and compared with several samples of $(PbSe)_{1-x}(PbS)_x$ doped with Pb up to 3.5×10^{19} cm^{-3}, $PbCl_2$ up to 4.5×10^{19} cm^{-3}, and Bi up to 7×10^{19} cm^{-3}. The calculation is in excellent agreement with the experimentally determined values, suggesting that electron scattering is not greatly affected by nanostructuring with PbS (see below), our selection of dopants, or the level of doping used. Therefore, a marked effect of doping on the density of states of the PbSe matrix (as for example in the case of Tl in PbTe[5,38,39]) is not anticipated.

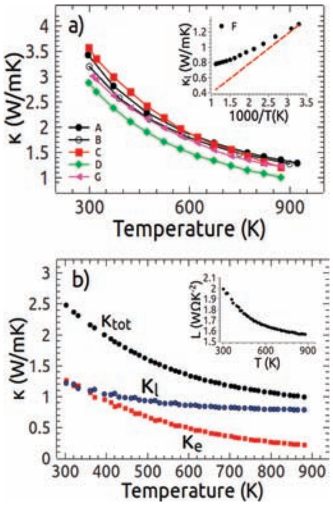

Figure 6. (a) Typical total thermal conductivity curves as a function of temperature measured on disk-shaped specimens of samples A, B, C, D, and G. The inset depicts the lattice thermal conductivity of sample F plotted against 1000/T. Note that the expected umklapp-dominated linear drop is not observed (red dashed line used as a guide) at high temperatures. (b) Calculated electronic, κ_e, and lattice, κ_l, contributions to the total thermal conductivity, κ_{tot}, of sample F. The inset shows the Lorenz number used in the calculations. The behavior is typical of all the specimens studied.

Figure 5 presents typical power factors, $S^2\sigma$, derived from the data of Figures 3a and 4a. The power factors are higher than those observed for Pb-doped PbSe at 900 K,[20] i.e., 11−14 μW/cm·K^2 at 900 K. The Bi-doped samples seem to have a marginally lower power factor related to a lower electrical conductivity at high temperature, probably due to the effects of grain boundaries and a greater tendency for microcracking.

3. Thermal Conductivity. Typical total thermal conductivity data are shown as a function of temperature in Figure 6a for 8% and 12% PbS compositions and all dopants. The κ_{tot} consists of the contributions of charge carriers and the lattice, and it decreases with increasing temperature. The data in Figure 6a correlate well with the results of Table 1, i.e. the higher the carrier density, the higher the thermal conductivity. Here sample G has a higher thermal conductivity compared to sample D, despite the similar electrical conductivity. This may be due to a lower density of mobility-limiting defects on the thermal diffusivity piece which was formed from the bottom part of the ingot.

To elucidate the contribution of the two components to the observed κ_{tot}, i.e. lattice and free carrier contributions, we have extracted the electronic thermal conductivities, $\kappa_{el} = L\sigma T$, based on fittings of the respective Seebeck coefficient values that in turn give better estimates of the Lorenz number, L, as explained in detail previously.[15,20] A typical example of such results is depicted in Figure 6b. The inset of Figure 6a shows a typical example where κ_l of sample F ($(PbSe)_{0.84}(PbS)_{0.16}$: $PbCl_2$ 0.3%) is plotted against $10^3/T$. The dashed red line represents the expected Debye−Peierls dependence with the same starting point as the room-temperature value, i.e., ~1.3 W/mK. As expected, the thermal conductivity of mixtures of PbSe and PbS is significantly lower compared to the room-temperature values of pristine PbSe (~1.9 W/mK),[20] pristine

PbS (~2.4 W/mK),[15] and also PbTe (~2.2 W/mK).[8] As evident from the inset of Figure 6a, the κ_l of sample F deviates from the expected T^{-1} of the Debye–Peierls prediction for $T > \Theta_D$,[34,40] where Θ_D is the Debye temperature ($\Theta_D^{PbSe} \approx 160$ K,[8] $\Theta_D^{PbS} \approx 220$ K[8]).

A significant difference between PbTe, PbSe, and PbS is an increase of the Grüneisen parameter when moving from tellurium to sulfur in the anionic sublattice.[8] Increasing the Grüneisen parameter increases anharmonicity in the lattice and hence the excitation of optical phonons.[8,40] In general, optical phonons excited in systems with a large Grüneisen parameter may or may not increase the thermal conductivity, depending on their dispersion and energy separation from the acoustic phonons and hence their interaction with acoustical-type phonons.[8] In fact, if the optical phonons are of sufficiently low dispersion and interact strongly with acoustical phonons, then an overall reduction in the thermal conductivity is expected, similar to the case of $AgSbTe_2$[41] and Si[42] (Si has a κ_l temperature dependence of $\sim 1/T^{1+x}$ for this reason). However, in PbTe, PbSe, and PbS this is hardly the case.[43] The Debye–Peierls prediction for a T^{-1} reduction in temperature is followed only by PbTe, suggesting only small involvement of optical phonon scattering. In contrast, PbSe and PbS exhibit exponential behavior with temperature of the form T^{-n}, with $n = 0.7–0.9$, which results in a higher lattice thermal conductivity at high temperatures compared to PbTe,[43] as shown in the inset of Figure 5. This excess lattice thermal conductivity could be the result of extra heat flow mediated through optical phonons. Alekseeva et al. observed the additive effect of optical phonons on the lattice thermal conductivity from a very low temperature,[43] in agreement with later reports of optical phonon effects on E_g of PbSe close to the Debye temperature.[44] Such effects may also be associated with the increasing displacement of Pb atoms from the octahedron center in the rock salt structure, as discovered recently in PbQ.[35] On the assumption that the lattice thermal conductivity of PbSe and PbS is the sum two components, acoustical and optical, the following formula, which describes the available experimental data, was suggested:[43]

$$\kappa_L = \frac{a}{T} + \beta\left(e^{-\hbar\omega_0/k_B T} - e^{-\hbar\omega_1/k_B T}\right) \tag{3}$$

The energies $\hbar\omega_0$ and $\hbar\omega_1$ in eq 3 correspond to the minimum and maximum optical phonon frequencies, and α and β are proportionality coefficients. Fitting our lattice thermal conductivity data on PbSe published in ref 15, we have extracted 12.4 meV (150 K) and 89.4 meV (~990 K) as the minimum and maximum optical phonon energies and $\beta \approx 0.47$ W/mK that lead to a room-temperature optical phonon contribution of ~17%, while at 900 K the contribution is ~50%. A similar analysis of data measured on undoped PbS crystals grown by the Bridgman method revealed an average functional dependence of the lattice thermal conductivity on temperature of $\sim T^{-0.75}$. Analyzing the data with eq 3, we find 7.9 meV (~90 K) and 91.7 meV (~1100 K) as the minimum and maximum optical phonon energies and $\beta \approx 0.68$ W/mK. These values lead us to estimate that optical phonons carry ~25% of heat in the lattice of PbS at room temperature and this percentage increases to ~64% at 900 K. This indicates that optical phonon conduction in the temperature range 300–900 K is an inherent effect of the lighter Pb chalcogenides.

In order to quantify the contribution of PbS to the reduction of the thermal conductivity of the $(PbSe)_{1-x}(PbS)_x$ system, we have used the KD theory of disordered alloys.[28,45] KD assumes scattering by point defects and umklapp processes alone, and it works well in predicting the lattice thermal conductivity in solid solution systems.[28] On the assumption of a Debye model of vibrations, the lattice thermal conductivity κ_L of a solid solution at $T > \Theta_D$ is given by

$$\kappa_L = \kappa_u \tan^{-1} y/y \tag{4}$$

where κ_u is the thermal conductivity due to umklapp processes and y is defined by the equation

$$y = \frac{\pi^2 \kappa_u \Theta_D \Omega}{h v^2}\Gamma \tag{5}$$

In the above equation, Ω is the average volume per atom, v is the average lattice sound velocity, and Γ is the disorder scaling parameter that depends on mass and strain field fluctuations that are taken to have an additive effect on Γ.[45] The mass fluctuations are quantified by Γ_M, which takes into account the average mass of each of the sublattices, and the strain field fluctuations by Γ_S, which is a value weighted by the average sublattice mass, the average sublattice ionic radius, and a phenomenological parameter ε.[45] The parameter ε is a function of the Grüneisen parameter and hence is a measure of the anharmonic contributions to the lattice.[46] The explicit relations of Γ_M and Γ_S given by Yang et al.[45] are

$$\Gamma_M = \frac{\sum_{i=1}^{n} c_i \left(\frac{\langle M_i\rangle}{M}\right)^2 f_i^1 f_i^2 \left(\frac{M_i^1 - M_i^2}{\langle M_i\rangle}\right)^2}{\sum_{i=1}^{n} c_i} \tag{6}$$

$$\Gamma_S = \frac{\sum_{i=1}^{n} c_i \left(\frac{\langle M_i\rangle}{M}\right)^2 f_i^1 f_i^2 \varepsilon_i \left(\frac{r_i^1 - r_i^2}{\langle r_i\rangle}\right)^2}{\sum_{i=1}^{n} c_i} \tag{7}$$

In eqs 6 and 7, c_i is the degeneracy (here $c_1 = c_2 = 1$), f_i the fractional occupation, $\langle r_i\rangle$ the average radius, $\langle M_i\rangle$ the average mass of each sublattice, and M the average atomic mass of the compound.

Equations 4 and 5 depend strongly on ε through Γ_S ($\Gamma = \Gamma_M + \Gamma_S$), and thus a well-educated assumption about ε is required rather than varying it as an adjustable parameter.[45,46] In our case we used published data of thermal conductivity for $PbSe_{1-x}Te_x$ solid solutions[8] to estimate the ε value as ~49. This is relatively close to $\varepsilon = 65$ generally assumed for PbTe.[47] For $\Theta_D \approx 160$ K, an average sound velocity similar to that for PbTe, $v \approx 1900$ m/s,[16,48] and using the atomic radii for Pb, Se, and S in a six-coordinate environment,[49] we have calculated the solid line shown in Figure 7. The black squares in Figure 7 correspond to measured undoped $(PbSe)_{1-x}(PbS)_x$ samples with a low carrier density. The electrical conductivity and thermopower of the samples were measured separately and used in evaluating the Lorenz number and the electronic component of the thermal conductivity, $\kappa_{el} = L\sigma T$, according to the procedure outlined previously.[15,20] It is clear from Figure 7 that the solid solution line lies well above the experimental data points by 0.2–0.4 W/mK, corresponding to ~15% difference. Postannealing of the undoped samples at 900 K for 72 h had no measurable effect on the reported room-temperature properties. Therefore, the additional ~15% difference between solid

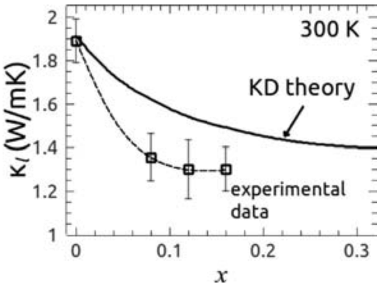

Figure 7. Lattice thermal conductivity (open squares and dashed line) of $(PbSe)_{1-x}(PbS)_x$ as a function of x measured in undoped ingots at room temperature. Error bars are indicated. The Seebeck coefficient and the electrical conductivity from these samples were used to accurately extract the electronic component. The black solid line corresponds to the prediction of Klemens−Drabble theory on the lattice thermal conductivity of solid solution alloys. The disagreement between theory and experiment is explained by the observed nanostructuring in the system that enhances acoustical phonon scattering (see text).

solution theory and experimental data arises from other factors, and this issue will be addressed shortly.

We note that similar quantitative differences between the calculated KD line and experimental data were observed by Irie[28] in PbTe−$AgSbTe_2$ and SnTe−$AgSbTe_2$, i.e., systems that despite showing a linear variation in their cubic lattice parameter ultimately were unequivocally shown to be nanostructured.[50−52] Consequently, the disagreement between KD theory and experiment, which was largely considered to be part of the uncertainty of the calculation and the experiment,[28] can now be understood on the basis of TEM observations.[51,52] Therefore, the thermal conductivity analysis presented above necessitates a careful examination of the microstructure of the system to investigate the existence of nanostructuring. This investigation is presented below.

4. Microstructure: Transmission Electron Microscopy. Figure 8 shows TEM observations of $(PbSe)_{1-x}(PbS)_x$ specimens. A detailed investigation of the system verified the presence of nanoscale regular spherical and plate-like precipitates in three samples, $(PbSe)_{1-x}(PbS)_x$ (x = 0.08, 0.12, and 0.16). The number density of the nanoscale precipitates increases with increasing PbS fraction. A high number density of plate-like precipitates was observed for $(PbSe)_{1-x}(PbS)_x$ (x = 0.16). This observation highlights the importance of electron microscopy in the accurate determination of the microstructure of materials rather than relying on experiments that are insensitive to nanoscale effects and give an "average" picture. Following the examples of PbTe−$AgSbTe_2$ and SnTe−$AgSbTe_2$,[50−52] PbSe−PbS is yet another example of a perceived solid solution that in fact is inhomogeneous on the nanoscale. These results reinforce the growing belief that complete solid solutions in semiconductors may be the exception rather than the rule. Future work on such systems should place equal onus and scrutiny on proving that a semiconductors alloy is in fact a solid solution, as we have done and others are now doing,[53−55] in showing the presence of nanostructuring.

It should be noted that ion beam thinning artifacts usually include mixing of nanostructures with the matrix rather than its formation. Thus, very thin edges of TEM foils are typically devoid of precipitates due to ion-beam-induced amorphization of the crystalline regions around the section hole. It is highly unlikely that ion beam thinning at cryogenic temperature would result in precipitate formation in an otherwise homogeneous matrix. Nevertheless, we have also employed alternate methods of specimen preparation, such as mechanical crushing to make cleaved sections of tiny particles, very low energy ion milling (at cryogenic temperatures), and FIB methods to ensure that formation of precipitates is intrinsic to this system rather than due to any specimen preparation artifacts.

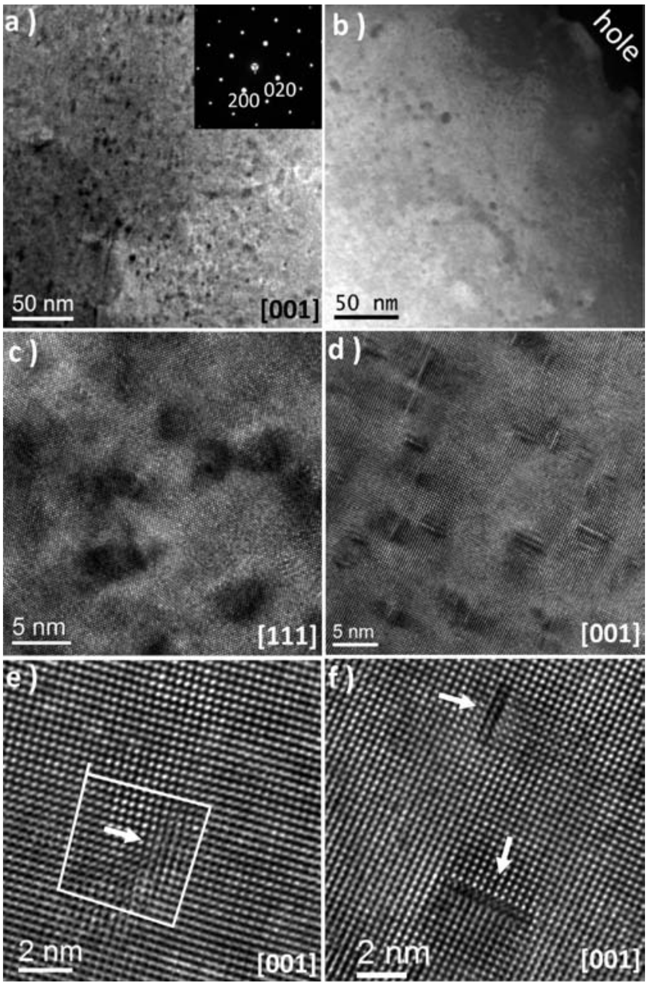

Figure 8. Low-magnification (a) bright-field TEM image of $(PbSe)_{1-x}(PbS)_x$ (x = 0.08) and (b) STEM image of $(PbSe)_{1-x}(PbS)_x$ (x = 0.16), showing spherical and plate-like PbS precipitates with a dark contrast embedded in the PbSe matrix. Inset: [001] electron diffraction pattern including the precipitates and matrix, which shows the absence of splitting of Bragg spots. Medium-magnification images of (c) $(PbSe)_{1-x}(PbS)_x$ (x = 0.12) and (d) $(PbSe)_{1-x}(PbS)_x$ (x = 0.16), clearly depicting matrix and two types of precipitates. (e) High-resolution image of $(PbSe)_{1-x}(PbS)_x$ (x = 0.08), showing a typical dislocation with Burger vector with $a/2$ [010]. (f) Lattice image of $(PbSe)_{1-x}(PbS)_x$ (x = 0.16), depicting two types of plate-like precipitates.

Figure 8a,b shows typical low-magnification S/TEM images of the $(PbSe)_{1-x}(PbS)_x$ (x = 0.08 and 0.16) samples. A high density of spherical inclusions with dark contrast is shown in Figure 8a; however, plate-like precipitates have a rather high number density in Figure 8b. Both types of inclusions have size distributions of 2−10 nm in the matrix. The inset of Figure 8a shows an electron diffraction pattern with the selected area aperture including the precipitates and the PbSe matrix recorded along [001] direction, which does not show split Bragg spots. The

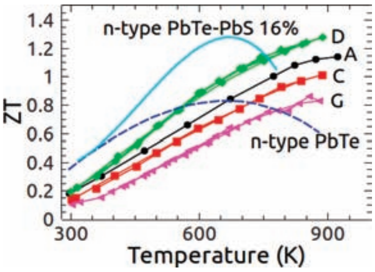

Figure 9. Figures of merit, ZT, as a function of temperature for samples A, C, D, and G compared to n-type PbTe-PbS 16% (data from ref 21) and optimized n-type PbTe (data from ref 57). The $(PbSe)_{1-x}(PbS)_x$ samples outperform PbTe and PbTe−PbS at 900 K.

medium-magnification images of samples $(PbSe)_{1-x}(PbS)_x$ ($x = 0.12$) (Figure 8c) and $(PbSe)_{1-x}(PbS)_x$ ($x = 0.16$) (Figure 8d) depict two types of precipitates (dark spots and lines) and reveal the formation of coherent or semicoherent interfaces.

Given the nanoscale nature of the precipitates and corresponding beam broadening effect in electron−specimen interactions, it is exceedingly difficult to unambiguously determine the quantitative chemical analysis of individual precipitates. That notwithstanding, X-ray dispersive spectroscopy (EDS) analysis of the dark areas showed a higher sulfur concentration with respect to the matrix, indicating the precipitates are endotaxially embedded PbS nanocrystals. In the sample $(PbSe)_{1-x}(PbS)_x$ ($x = 0.08$), we also observed medium-density dislocations in the PbSe matrix, as shown in Figure 8e. The Burger's circuit around the dislocation core yields a closure failure with a projected vector of $a/2\,[010]$. In Figure 8f, the lattice image of PbSe−PbS 16% shows two types of plate-like precipitates at atomic resolution level. The top one has two layers with dark contrast compared to the PbSe matrix, but the bottom one has a smaller lattice parameter, 45° rotation compared to the matrix, and also shifts in the lattice of both sides close to the precipitate, which is similar to previous observations in the Pb-doped PbTe system.[56]

The nanoscale spherical and plate-like PbS precipitates are dispersed through the matrix in all samples. The observation of plate-like and spherical precipitates points to additional scattering mechanisms arising from the matrix−nanocrystal interface, which can explain the difference of KD theory when compared to experimental thermal conductivity. Despite this nanoscale phase inhomogeneity, we note that there is still significant solid solution mixing in the respective phases, given that the lattice mismatch is only 3.1%. In the matrix of PbSe there is a dissolved fraction of PbS, and vice versa in the precipitates of PbS. Therefore, a more descriptive formula of the nominal $(PbSe)_{1-x}(PbS)_x$ system is $[(PbSe_{1-y}S_y)]_{1-z}[PbS_{1-y}Se_y]_z$, where y is the lattice dissolved fraction and z is the precipitated fraction (i.e., $x = z + y$). Nanostructuring can also explain the doping trend observed in samples C, D, and F (see Table 1) that have the same dopant $PbCl_2$ concentration but different PbS fractions. Upon PbS precipitation, which increases with increasing S content according to the TEM results, an excess $PbCl_2$ remains that cannot be accommodated by the remaining Se-rich matrix and thus escapes, reducing the carrier density. Interestingly, for every 4% increment increase in PbS concentration, a $\Delta n \approx 0.4 \times 10^{19}$ incremental decrease in carrier density is observed.

Despite the competing effect of optical phonon-mediated heat transport, the reduction in the thermal conductivity is still significant enough to realize figures of merit higher than unity at 900 K. Figure 9 depicts our results as a function of temperature, where ZT ≈ 1.3 was achieved at 900 K and compared to nanostructured n-type $(PbTe)_{0.84}(PbS)_{0.16}$[21] and optimized n-type PbTe.[57] The results presented in Figure 9 have been repeated in three more samples. Since PbTe exhibits bipolar diffusion effects at temperatures higher than 700 K, the ZT peaks around that temperature and is subsequently reduced. As a result, $(PbSe)_{1-x}(PbS)_x$ outperforms PbTe and PbTe−PbS at 900 K. Given the fact that the efficiency of thermoelectric devices, η_{TE}, depends not only on ZT but also on the temperature difference of the hot, T_H, and cold, T_C, junctions under operation conditions through the equation

$$\eta_{TE} = \frac{T_H - T_C}{T_H}\,\frac{\sqrt{1+ZT}-1}{\sqrt{1+ZT}+\dfrac{T_C}{T_H}} \tag{8}$$

the reported results hold great promise for conversion efficiencies similar to those obtained with the advanced nanostructured PbTe-based materials.

CONCLUDING REMARKS

We have provided the first evidence that the system $(PbSe)_{1-x}(PbS)_x$, widely believed to be a solid solution, is in fact nanostructured. The self-forming nanostructuring plays a significant role in decreasing the thermal conductivity and therefore is an important parameter that can be carefully tuned to achieve further increases in ZT. Appropriate choice of dopants and carrier optimization can be combined with the overall lower thermal conductivity to give ZT ≈ 1.3 at 900 K. The inherent effect of optical phonon excitations in PbSe and PbS may account for the lower efficiency of nanostructuring in reducing the lattice thermal conductivity compared to the PbTe−PbS system.[21−23] In PbTe the contribution of optical phonons to the thermal conductivity is small, whereas in $(PbSe)_{1-x}(PbS)_x$ it is significant and acts to partially mitigate the effects of nanostructuring. Nevertheless, the present and recent[15,20] results in combination constitute a significant step forward in de-tellurizing thermoelectric materials for waste heat energy harvesting. From these results, it is apparent that PbSe- and PbS-based materials are promising less expensive alternatives to PbTe and have the potential to produce energy conversion devices with similar or superior thermoelectric performance.

AUTHOR INFORMATION

Corresponding Author

m-kanatzidis@northwestern.edu

ACKNOWLEDGMENT

We thank Dr. Simon Johnsen for providing us with PbS lattice thermal conductivity data. This material is based upon work supported as part of the Revolutionary Materials for Solid State Energy Conversion, an Energy Frontier Research Center funded by the U.S. Department of Energy, Office of Science, Office of Basic Energy Sciences, under Award No. DE-SC0001054. This work was also supported by the U.S. Department of Energy, Office of Science, under Contract No. DE-AC02-06CH11357. TEM work was performed in the EPIC/NIFTI/Keck-II facility of the NUANCE Center at Northwestern University. The NUANCE Center is supported by NSF-NSEC, NSF-MRSEC, Keck Foundation, the State of Illinois, and Northwestern University.

REFERENCES

(1) Kanatzidis, M. G. *Chem. Mater.* **2010**, *22*, 648.

(2) Sootsman, J. R.; Chung, D. Y; Kanatzidis, M. G. *Angew. Chem., Int. Ed.* **2009**, *48*, 8616.

(3) Szczech, J. R.; Higgins, J. M.; Jin, S. *J. Mater. Chem.* **2011**, *21*, 4037.

(4) Dresselhaus, M. S.; Chen, G.; Tang, M. Y.; Yang, R. G.; Lee, H.; Wang, D. Z.; Ren, Z. F.; Fleurial, J.-P; Gogna, P. *Adv. Mater.* **2007**, *19*, 1043.

(5) Heremans, J. P.; Jovovic, V.; Toberer, E. S.; Saramat, A.; Kurosaki, K.; Charoenphakdee, A.; Yamanaka, S.; Snyder, G. J. *Science* **2008**, *321*, 554.

(6) Hu, Z. C.; Gao, S. *Chem. Geol.* **2008**, *253*, 205.

(7) George, M. W. *Mineral Yearbook 2007: Selenium and Tellurium*; U.S. Geological Survey: Washington, DC, 2007.

(8) Ravich, I. I.; Efimova, B. A.; Smirnov, I. A., *Semiconducting lead chalcogenides*; Plenum Press: New York, 1970.

(9) Parker, D.; Singh, D. J. *Phys. Rev. B* **2010**, *82*, 035204.

(10) (a) Ahn, K.; Han, M. K.; He, J. Q.; Androulakis, J.; Ballikaya, S.; Uher, C.; Dravid, V. P.; Kanatzidis, M. G. *J. Am. Chem. Soc.* **2010**, *132*, 5227–5235. (b) He, J. Q.; Sootsman, J. R.; Xu, L. Q.; Girard, S. N.; Zheng, J. C.; Kanatzidis, M. G.; Dravid, V. P. *J. Am. Chem. Soc.* **2011**, *133*, 8786–8789.

(11) Androulakis, J.; Todorov, I.; Chung, D. Y.; Ballikaya, S.; Wang, G. Y.; Uher, C.; Kanatzidis, M. *Phys. Rev. B* **2010**, *82*, 115209.

(12) Biswas, K.; He, J. Q.; Zhang, Q. C.; Wang, G. Y.; Uher, C.; Dravid, V. P.; Kanatzidis, M. G. *Nature Chem.* **2011**, *3*, 160–166.

(13) Kumar, R. S.; Balasubramanian, M.; Jacobsen, M.; Bommannavar, A.; Kanatzidis, M.; Yoneda, S.; Cornelius, A. L. *J. Electron. Mater.* **2010**, *39*, 1828–1831.

(14) Vineis, C. J.; Shakouri, A.; Majumdar, A.; Kanatzidis, M. G. *Adv. Mater.* **2010**, *22*, 3970–3980.

(15) (a) Johnsen, S.; He, J.; Androulakis, J.; Dravid, V. P.; Todorov, I.; Chung, D.-Y.; Kanatzidis, M. *J. Am. Chem. Soc.* **2011**, *133*, 3460. (b) Lioutas, C. B.; Frangis, N.; Todorov, I.; Chung, D. Y.; Kanatzidis, M. G. *Chem. Mater.* **2010**, *22*, 5630–5635.

(16) Wang, H.; Pei, Y.; LaLonde, A. D.; Snyder, G. J. *Adv. Mater.* **2011**, *23*, 1366.

(17) Sakamoto, T.; Iida, T.; Matsumoto, A.; Honda, Y.; Nemoto, T.; Sato, J.; Nakajima, T.; Taguchi, H.; Takanashi, Y. *J. Electron. Mater.* **2010**, *39*, 1708.

(18) Rogl, G.; Grytsiv, A.; Rogl, P.; Bauer, E.; Kerber, M. B.; Zehetbauer, M.; Puchegger, S. *Intermetallics* **2010**, *18*, 2435.

(19) Kim, H.; Kaviany, M.; Thomas, J. C.; Van der Vev, A.; Uher, C.; Huang, B. L. *Phys. Rev. Lett.* **2010**, *105*, 265901.

(20) Androulakis, J.; Lee, Y.; Todorov, I.; Chung, D.-Y.; Kanatzidis, M. *Phys. Rev. B* **2011**, *83*, 195209.

(21) Androulakis, J.; Lin, C.-H.; Kong, H.-J.; Uher, C.; Wu, C.-I.; Hogan, T.; Cook, B. A.; Caillat, T.; Paraskevopoulos, K. M.; Kanatzidis, M. G. *J. Am. Chem. Soc.* **2007**, *129*, 9780.

(22) Girard, S. N.; He, J.; Li, C.; Moses, S.; Wang, G.; Uher, C.; Dravid, V. P.; Kanatzidis, M. G. *Nano Lett.* **2010**, *10*, 2825.

(23) He, J.; Girard, S. N.; Kanatzidis, M. G.; Dravid, V. P. *Adv. Funct. Mater.* **2010**, *20*, 764.

(24) Schlichting, U.; Gobrecht, K. *J. Phys. Chem. Solids* **1973**, *34*, 753.

(25) Veĭs, A. N.; Kaĭdanov, V. I.; Nemov, S. A. *Sov. Phys. Semicond.* **1980**, *14*, 628.

(26) Volykhov, A. A.; Yashina, L. V.; Shtanov, V. I. *Inorg. Mater.* **2006**, *42*, 596.

(27) Scanlon, W. W. *J. Phys. Chem. Solids* **1959**, *8*, 423.

(28) Irie, T. *Jpn. J. Appl. Phys.* **1966**, *5*, 854.

(29) Blachnik, R.; Igel, R. *Z. Naturforsch. B* **1974**, *29*, 625.

(30) Neuelemann, R.; Marino, A.; Reichelt, K. *J. Cryst. Growth* **1983**, *64*, 609.

(31) Lach-hab, M.; Papaconstantopoulos, D. A.; Mehl, M. J. *J. Phys. Chem. Solids* **2002**, *63*, 833.

(32) Hoang, K.; Mahanti, S. D.; Jena, P. *Phys. Rev. B* **2007**, *76*, 115432.

(33) Smirnov, I. A.; Moizhes, B. Y.; Nensberg, E. D. *Sov. Phys. Solid State* **1961**, *2*, 1793.

(34) Goldsmid, H. J., *Introduction to Thermoelectricity*; Spinger Series in Materials Science; Springer: Heidelberg, 2010.

(35) Bozin, E.; Malliakas, C. D.; Souvatzis, P.; Proffen, T.; Spaldin, N. A.; Kanatzidis, M. G.; Billinge, S. J. L. *Science* **2010**, *330*, 1660.

(36) Fistul',V. I., *Heavily doped semiconductors*; Plenum Press: New York, 1969.

(37) Aziza, A.; Amzallag, E.; Balkanski, M. *Solid State Commun.* **1970**, *8*, 873.

(38) Kaĭdanov, V. I.; Ravich, Yu. I. *Sov. Phys. Usp.* **1985**, *28*, 31.

(39) Nemov, S. A.; Ravich, Yu. I. *Phys. Usp.* **1998**, *41*, 735.

(40) Yang, J. In *Thermal Conductivity*; Tritt, T. M., Ed.; Kluwer Academic/Plenum Press: New York, 2004.

(41) Morelli, D. T.; Jovovic, V.; Heremans, J. P. *Phys. Rev. Lett.* **2008**, *101*, 035901.

(42) Glassbrenner, C. J.; Slack, G. A. *Phys. Rev.* **1964**, *134*, A1058.

(43) Alekseeva, G. T.; Krylov, E. T. *Sov. Phys. Solid State* **1984**, *25*, 2140.

(44) Baleva, M.; Georgiev, T.; Lashkarev, G. *J. Phys.:Condens. Matter* **1990**, *1*, 2935.

(45) Yang, J.; Meisner, G. P.; Chen, L. *Appl. Phys. Lett.* **2004**, *85*, 1140.

(46) Abeles, B. *Phys. Rev.* **1963**, *131*, 1906.

(47) Alekseeva, G. T.; Efimova, B. A.; Ostrovskaya, L. M.; Serebryannikova, O. S.; Tsypin, M. I. *Sov. Phys. Semicond.* **1971**, *4*, 1122.

(48) Ren, F.; Case, E. D.; Ni, J. E.; Timm, E. J.; Lara-Curzio, E.; Trejo, R. M.; Lin, C. H.; Kanatzidis, M. G. *Philos. Mag.* **2009**, *89*, 43.

(49) Shannon, R. D. *Acta Crystallogr. A* **1976**, *32*, 751.

(50) Hsu, K.-F.; Loo, S.; Guo, F.; Chen, W.; Dyck, J. S.; Uher, C.; Hogan, T.; Polychroniadis, E. K.; Kanatzidis, M. G. *Science* **2004**, *303*, 818.

(51) Quarez, E.; Hsu, K.-F.; Pcionek, R.; Frangis, N.; Polychroniadis, E. K.; Kanatzidis, M. G. *J. Am. Chem. Soc.* **2005**, *127*, 9177.

(52) Androulakis, J.; Pcionek, R.; Quarez, E.; Do, J. H.; Kong, H. J.; Palchik, O.; Uher, C.; D'Angelo, J. J.; Short, J.; Hogan, T.; Kanatzidis, M. G. *Chem. Mater.* **2006**, *18*, 4719.

(53) Pei, Y.; Lensch-Falk, J.; Toberer, E.; Medlin, D. L.; Snyder, G. J. *Adv. Funct. Mater.* **2010**, *21*, 241.

(54) Ikeda, T.; Collins, L. A.; Ravi, V. A.; Gascoin, F. S.; Haile, S. M.; Snyder, G. J. *Chem. Mater.* **2007**, *19*, 763.

(55) Zhu, T.-J.; Cao, Y.-Q.; Zhang, Q.; Zhao, X.-B. *J. Electron. Mater.* **2009**, *39*, 1990.

(56) He, J.; Sootsman, J. R.; Girard, S. N.; Zheng, J.; Wen, J.; Zhu, Y.; Kanatzidis, M. G.; Dravid, V. P. *J. Am. Chem. Soc.* **2010**, *132*, 8669.

(57) Wood, C. *Energy Convers. Manage* **1984**, *24*, 331.